

The HELLAS2XMM survey

III. Multiwavelength observations of hard X-ray selected sources in the PKS 0312–77 field*

M. Brusa^{1,2}, A. Comastri², M. Mignoli², F. Fiore³, P. Ciliegi², C. Vignali^{2,4}, P. Severgnini⁵, F. Cocchia³, F. La Franca⁶, G. Matt⁶, G. C. Perola⁶, R. Maiolino⁷, A. Baldi⁸, and S. Molendi⁸

¹ Dipartimento di Astronomia Università di Bologna, via Ranzani 1, 40127 Bologna, Italy
e-mail: brusa@bo.astro.it

² INAF – Osservatorio Astronomico di Bologna, via Ranzani 1, 40127 Bologna, Italy
e-mail: comastri,mignoli,ciliegi@bo.astro.it

³ INAF – Osservatorio Astronomico di Roma, via Frascati 33, 00040 Monteporzio, Italy
e-mail: fiore,cocchia@quasar.mporzio.astro.it

⁴ Department of Astronomy and Astrophysics, The Pennsylvania State University, 525 Davey Lab, University Park, PA 16802, USA
e-mail: chris@astro.psu.edu

⁵ INAF – Osservatorio Astronomico di Brera, via Brera 28, 20121 Milano, Italy
e-mail: paola@brera.mi.astro.it

⁶ Dipartimento di Fisica Università di Roma Tre, via della Vasca Navale 84, 00146 Roma, Italy
e-mail: lafranca,matt,perola@fis.uniroma3.it

⁷ INAF – Osservatorio Astrofisico di Arcetri, Largo E. Fermi 5, 50125, Firenze, Italy
e-mail: maiolino@arcetri.astro.it

⁸ IASF – CNR, Istituto di Fisica Cosmica, via Bassini 15, 20133, Milano, Italy
e-mail: baldi,molendi@mi.iasf.cnr.it

Received 6 March 2003 / Accepted 11 July 2003

Abstract. We present extensive optical, radio and infrared follow-up observations of a sample of 35 hard X-ray (2–10 keV) selected sources discovered serendipitously in the PV XMM–*Newton* observation of the radio-loud quasar PKS 0312–77 field, for which also an archival *Chandra* observation is available. The observations have been carried out as part of the HELLAS2XMM survey, a program aimed to understand the nature of the sources responsible for the bulk of the hard X-ray Background (XRB). The identification of the optical counterparts greatly benefits from the positional accuracy obtained from *Chandra* and radio observations. As a consequence, the spectroscopic completeness of the present sample (80%) is limited only by the faintness of the optical counterparts. The multiwavelength coverage of our survey allows us to unveil a large spread in the overall properties of hard X-ray selected sources. At low redshift ($z < 1$), the source breakdown includes Broad Line AGN, Narrow Emission-Line Galaxies, and optically “normal” galaxies. All the ten sources at $z > 1$ are spectroscopically classified as Broad Line AGNs. A few of them show significant intrinsic X-ray absorption ($N_{\text{H}} > 10^{22} \text{ cm}^{-2}$), further supporting previous evidence of a decoupling between optical and X-ray properties at high luminosities and redshifts. Finally, a non negligible fraction (~15%) of the hard X-ray sources are not detected down to the limiting magnitude of the optical images. The corresponding high X-ray to optical flux ratio, X-ray and optical–infrared colors strongly suggest that they are high redshift, obscured AGN.

Key words. surveys – galaxies: active – X-ray: galaxies – X-rays: general – X-rays: diffuse background

Send offprint requests to: M. Brusa,
e-mail: brusa@bo.astro.it

* This work is based on observations collected at the European Southern Observatory, La Silla, Chile (proposals ID: 66.A-0520(A), 67.A-0401(A), 68.A-0514(A)) and Paranal, Chile (proposal ID: 69.A-0506(A)), and observations made with the XMM–*Newton*, an ESA science mission with instruments and contributions directly funded by ESA member states and the USA (NASA)

1. Introduction

Deep X-ray surveys carried out with *Chandra* and XMM–*Newton* have resolved a large fraction (more than 80%) of the hard X-ray Background (XRB) into discrete sources (Mushotzky et al. 2000; Brandt et al. 2001; Alexander et al. 2003; Hasinger et al. 2001; Giacconi et al. 2001) down to a 2–10 keV flux limit of about $2 \times 10^{-16} \text{ erg cm}^{-2} \text{ s}^{-1}$.

The results of the optical identifications show that about half of the objects are associated with optically bright ($I < 24$) galaxies at redshifts < 1.5 which are often identified with Active Galactic Nuclei (AGN), while the other half appears to be a mixture of higher redshift AGN and optically faint ($I > 24$) galaxies (Alexander et al. 2001; Barger et al. 2001, 2002; Giacconi et al. 2002).

In order to better understand the nature of the various components of the X-ray background light we have started a program of multiwavelength follow-up observations of hard X-ray selected sources serendipitously discovered in 15 XMM-Newton fields over $\sim 3 \text{ deg}^2$ (the HELLAS2XMM survey; Baldi et al. 2002). The 2–10 keV sample of the HELLAS2XMM survey consists of 495 sources detected in the hard X-ray band at fluxes of the order of $\sim 10^{-14}$ – $10^{-12} \text{ erg cm}^{-2} \text{ s}^{-1}$ where a significant fraction of the XRB is resolved (~ 50 – 60% ; see, e.g., Comastri 2001 for a review) and at the same time the optical identification process is relatively easy. This strategy allows to cover a large area of the sky and to fill the gap between previous shallow hard X-ray surveys (the *BeppoSAX* HELLAS survey, Fiore et al. 2001; the ASCA GIS survey, Cagnoni et al. 1998; the ASCA LSS and MSS Surveys, Akiyama et al. 2000; Ueda et al. 1999; Akiyama et al. 2002) and recent deep *Chandra* (CDF-N, Brandt et al. 2001; CDF-S, Giacconi et al. 2002) and XMM-Newton (Lockman Hole, Hasinger et al. 2001) observations.

To date, we have performed an extensive optical follow-up program for about one third of the fields (Fiore et al. 2003). The final aim of this project is the derivation of an accurate luminosity function over a wide range of redshifts and luminosities for a large sample of hard X-ray selected, presumably obscured objects, in order to trace the accretion history in the Universe. Indeed, X-ray absorbed sources are a key parameter for AGN synthesis models of the XRB, which, in their simplest versions (Setti & Woltjer 1989; Madau et al. 1994; Comastri et al. 1995), predict a large number of high-luminosity, highly obscured quasars (the so-called QSO2). In the zeroth order unifications models, QSO2 are predicted to be the high-luminosity counterparts of local Seyfert 2 galaxies. Despite intensive optical searches, these narrow-line high-redshift objects appear to be elusive, suggesting a space density and evolution different from that expected from unified schemes and calling for substantial revision of the XRB baseline models (Gilli et al. 2001). However, the results of recent multi-wavelength follow-up from both shallow and deep surveys, indicate that the sources responsible for a large fraction of the XRB energy density are characterized by a large spread in their optical properties; therefore the understanding of the energetically dominant component of the XRB is possible only by means of multiwavelength observations.

In this framework, the field surrounding the radio-loud quasar PKS 0312–77 (one of the HELLAS2XMM fields) is a key example. It has been observed both by *Chandra* and XMM-Newton during their Calibration and Performance Verification (PV) phases; deep radio observations at 5 GHz have been obtained with the Australian Telescope Compact Array (ATCA) telescope, along with the optical imaging at the ESO 3.6 m telescope for the 35 objects detected in the combined

MOS1 + MOS2 + pn XMM-Newton observation. Optical spectroscopy has been obtained for 28 sources, both at the ESO 3.6 m and VLT/FORS1 telescopes.

In Sect. 2 we present the multiwavelength data, in Sect. 3 the X-ray sources identification, and in Sect. 4 the radio properties. In Sect. 5 we discuss the source breakdown and the multiwavelength properties of the sources. Finally, in Sect. 6 we summarize our results.

Throughout the paper, the adopted values for the Hubble constant and the cosmological parameters are $H_0 = 70 \text{ km s}^{-1} \text{ Mpc}^{-1}$, $\Omega_\Lambda = 0.7$, $\Omega_m = 0.3$.

2. Multiwavelength observations

2.1. XMM-Newton

The PKS 0312–77 field was observed during the XMM-Newton PV phase, in 2000, March 31, for a nominal exposure time of ~ 30 ks.

The XMM-Newton data were processed using version 5.3 of the Science Analysis System (SAS). The event files were cleaned up from hot pixels and soft proton flares (see Baldi et al. 2002 for details). The resulting exposure times are 24.7, 26.5 and 26.1 ks in the *pn*, *MOS1* and *MOS2* detectors, respectively.

The excellent relative astrometry between the three cameras (within $1''$, below their *FWHM* of $\sim 6''$) allows us to merge the *MOS* and *pn* images in order to increase the signal to noise ratio and to reach fainter X-ray fluxes.

An accurate detection algorithm developed by our group (Baldi et al. 2002) was run on the 2–10 keV cleaned event, in order to create a list of candidate sources. We then computed the probability that the detected counts originate from poissonian background fluctuations: 35 sources were detected above a detection threshold of $p = 2 \times 10^{-5}$. The count rate to flux conversion factor was derived assuming a power law with photon index $\Gamma = 1.7$, absorbed by the Galactic column density toward the PKS 0312–77 field ($N_H = 8 \times 10^{20} \text{ cm}^{-2}$, Dickey & Lockman 1990), and weighted by the effective exposure time of the different EPIC cameras. The uncertainty in the derived fluxes is $< 15\%$ for $\Delta\Gamma = \pm 0.5$. The 2–10 keV fluxes range from $\sim 1 \times 10^{-14}$ to $4 \times 10^{-13} \text{ erg cm}^{-2} \text{ s}^{-1}$.

The same detection algorithm was also run in the 0.5–2 keV energy range in order to characterize the average spectral properties of the sources in our sample using the hardness-ratio technique.

The XMM-Newton observation of the PKS 0312–77 field has been already analyzed by Lumb et al. (2001); the same dataset is included in the First XMM-Newton Serendipitous Source Catalogue (2003, version 1.0.1), recently released by the XMM-Newton Survey Science Centre¹ (SSC). A detailed comparison of the three samples is discussed in Appendix A.

2.2. Chandra

The PKS 0312–77 field was also observed by *Chandra* during a PV observation in 1999, September 8, for a total exposure time

¹ <http://xmmssc-www.star.le.ac.uk/>

of ~ 12 ks. The analysis of the six objects selected in the 2–10 keV band based on preliminary calibration data and detection techniques has been already reported by Fiore et al. (2000, hereinafter F00). Thanks to the unprecedented *Chandra* positional accuracy ($\sim 1''$), it was possible to unambiguously identify all of the optical counterparts of these hard X-ray sources.

An additional, almost simultaneous *Chandra* observation of the PKS 0312–77 field was retrieved from the archive, combined with the previous one, and analyzed using version 2.2 of the CXC software. The high-background intervals were filtered out leaving about 24.7 ksec of useful data. The WAVDETECT algorithm (Freeman et al. 2002) was run on the cleaned full band (0.5–8 keV) image setting a false-positive threshold of 10^{-7} , which led to highly reliable detections, as shown in the HDF-N field (e.g., Brandt et al. 2001).

Twenty-five out of the 35 XMM-Newton sources are within the *Chandra* ACIS-I field-of-view (FOV); only two sources detected in the XMM-Newton observation were not detected by *Chandra*: one object falls in a CCD gap, while the other is just below the adopted probability threshold.

A detailed analysis of the *Chandra* X-ray spectral properties and the comparison with the XMM-Newton results is prevented by the well known calibration problems related to the relatively high temperature of the ACIS-I detector during the PV phase. We made use of the extremely good positional accuracy provided by *Chandra* which allowed us to unambiguously estimate the X-ray centroid position for the 23 common sources (see Sect. 3).

2.3. Optical imaging

The optical imaging (*R*-Bessel filter) of the PKS 0312–77 field was carried out using EFOSC2 (Patat 1999) at the 3.6 m ESO telescope in La Silla during three different observing runs (periods 66–68). Exposure times were typically of 5–10 min, with a typical seeing of about $1.5''$. We acquired 16 *R*-band frames in order to cover all the X-ray sources; each single image, with a pixel size of 0.32 arcsec and a FOV of $\sim 5.3 \times 5.3$ square arcmin, was cross-matched to the USNO catalog² (Monet et al. 1998) and astrometrically calibrated using the package GAIA (version 2.3-1 driven P.W. Draper from the Skycat software developed by ESO). We obtained a good astrometric solution for each frame, with rms in each coordinate of about 0.1–0.2''. The images were reduced using standard techniques including de-bias, flat-fielding, and fringing correction (if needed). The photometric calibration was performed for each night using the zero-point derived from the measured instrumental magnitudes of standard stars and assuming the average extinction reported in the Observatory web page³.

The optical source catalogue was created using the SExtractor software (Bertin & Arnouts 1996). Since the images have been obtained under different seeing conditions, the limiting magnitude has been conservatively estimated in each frame as the 3σ (sky value) over 2.5 times the seeing area.

Using this definition, the limiting magnitudes range between 24.0 and 25.2, mainly depending on the image seeing.

2.4. Optical spectroscopy

The spectroscopic follow-up observations of the optically bright population (17 sources with $R < 22$) have been performed with the ESO 3.6 m telescope equipped with EFOSC2 during four different observing runs (Jan. 2000–Nov. 2001) in the framework of the identification program of the HELLAS2XMM survey. We used the EFOSC2 grism #13 with a 1.5 arcsec slit, which yields a dispersion of about 2.8 Å per pixel and provides a good spectral coverage up to 9000 Å. The exposure times vary between 600 and 2400 s, depending on the target magnitude. The spectroscopic follow-up of the 11 sources with $R = 22$ –24 has been performed with the ESO VLT/UT2 telescope equipped with FORS1 during period 69. The grism 150I with a 1.3 arcsec slit was used, providing a dispersion of 5.4 Å per pixel and a wide spectral domain ($\approx 3500 \div 10\,000$ Å). The FORS1 exposure times range from 480 up to 6300 s; dithering of the targets along the slits was applied for the faintest objects in order to optimally remove the fringing at wavelengths longer than 7500 Å.

All the spectroscopic data have been reduced using standard IRAF⁴ routines. Bias exposures taken on each night were stacked, checked for consistency with the overscan regions of spectroscopic frames, and subtracted out. The bias-subtracted frames were then flat-fielded in a standard manner using internal lamp flats obtained during the same run. The sky background was removed by fitting a third-order polynomial along the spatial direction in source free regions. In all the observing runs the wavelength calibration was made using arc lamps (He–Ar for the EFOSC2 data, He–Ar–Hg for the FORS1 data) and different spectroscopic standard stars were used for the flux calibration.

2.5. Radio

A deep radio observation of the PKS 0312–77 field at 5 GHz was performed with the Australian Telescope Compact Array (ATCA) in the 6-km configuration (maximum baseline length), with a synthesized beam size (HPBW) of $\sim 2''$. The data were collected in a 12-hours run on 2000, September 27. In order to improve the sensitivity by a factor of $\sqrt{2}$, we used both ATCA receivers at 5 GHz, centered at 4800 and 5824 MHz, respectively. The field was observed in the mosaic mode by cycling through a grid of 5 pointings on the sky, in order to yield a uniform noise over the area covered by the *Chandra* data.

The data were analyzed with the software package MIRIAD. Since the ATCA correlator provides a bandwidth of 128 MHz subdivided into 32 frequency channels (of 4 MHz each), in the data reduction we used the multi-frequency synthesis algorithms which give the opportunity of producing images with

² <http://archive.eso.org/skycat/servers/usnoa>

³ <http://www.eso.org/observing/support.html>

⁴ IRAF is distributed by the National Optical Astronomy Observatories, which is operated by the Association of Universities for Research in Astronomy, Inc, under cooperative agreement with the National Science Foundation.

improved (u, v) coverage by combining accurately the visibility of individual channels. The division of the wide passband into subchannels reduces the effects of bandwidth smearing. Each bandpass was calibrated and cleaned separately to produce two individual images that were combined together into a single mosaic at the end of the reduction phase. Self-calibration was used to make additional correction to the antenna gains and to improve the image quality. The final map has uniform noise of $50 \mu\text{Jy}$ (1σ) over an area with a semicircular shape (due to the odd numbers of pointings) with a radius of about 10 arcmin, surrounded by an area where the noise increases for increasing distance from the center. The accuracy on the radio position is of the order of $\sim 2''$ for the faintest objects.

2.6. Near-infrared

Deep K_s observations of a small subsample (ten objects) of the hard X-ray sources detected in the PKS 0312 field have been obtained with the Infrared Spectrometer And Array Camera (ISAAC, see Moorwood et al. 1999) mounted on the ESO VLT-UT1 telescope, as a part of complementary programs of the HELLAS2XMM survey. The observations have been collected in service mode during relatively good seeing conditions ($< 0.8''$). We used the ISAAC SW Imaging Mode, which gives a pixel scale of $0.1484 \text{ arcsec/pixel}$ and a FOV of 2.5×2.5 square arcmin. The net exposure time was 36 min for each field and, after running SExtractor, we estimated a 50% completeness at $K_s \approx 21$ by comparing our data with deeper surveys (e.g., Saracco et al. 2001; Bershadsky et al. 1998). The data reduction has been performed in two steps: individual raw frames have been first corrected for bias and dark current, and flat-fielded using standard IRAF routines. For the sky subtraction and image co-adding we then used DIMSUM⁵, a contributed package of IRAF.

The K -band imaging data are used only for what concern the identification of the X-ray counterparts (see Sect. 3). We refer to Mignoli et al. (in preparation) for a full discussion on data reduction and analysis techniques.

3. X-ray sources identification

At first, we have accounted for the astrometric calibration of the X-ray image by looking for average displacement of bright type 1 AGN already identified in F00. We found an average shift of $\sim 2''$ ($\Delta(\text{Ra}) = 1.67''$; $\Delta(\text{Dec}) = -1.13''$), in agreement with the findings reported in Lumb et al. (2001), where the astrometric calibration was done with respect to the position of the bright central target. We have also verified the effects of possible scale and rotational offsets in the matched astrometric solution, that turned out to be negligible. The uncertainties in the determination of the X-ray positions are mainly ascribed to the XMM-Newton PSF, in particular at faint X-ray fluxes where the statistical error in RA and Dec determination are expected to be in the range 1–2 arcsec (see Sect. 6.3 in the First

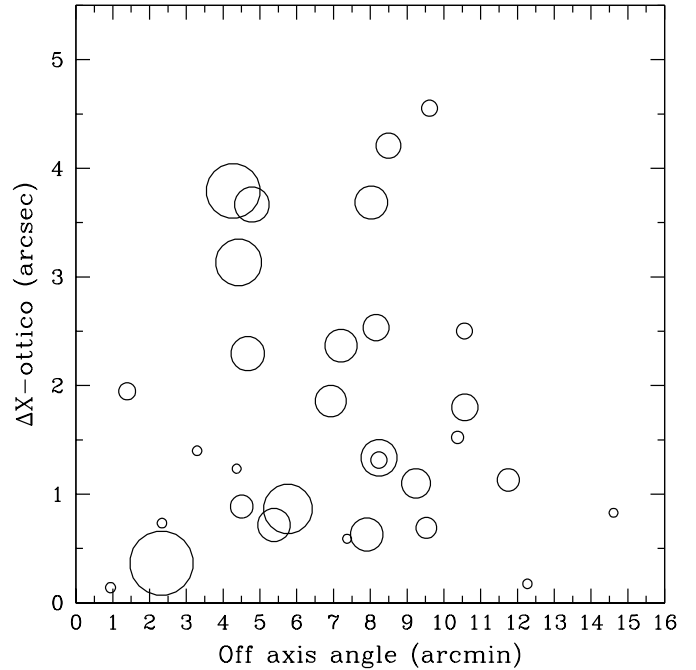


Fig. 1. Displacements between the optical and X-ray positions as a function of the off-axis angle. The size of the symbols increases as the X-ray flux decreases.

XMM-Newton Serendipitous Source Catalogue: 1XMM, User Guide to the Catalogue).

In order to accommodate any residual systematics in the astrometric calibration of the EPIC images (see Barcons et al. 2002) and to fully account for the PSF broadening in faint sources (e.g., sources with < 100 cts), we have searched for optical counterparts for all the X-ray sources within a conservative matching radius of 5 arcsec from the astrometrically corrected X-ray centroid. Such a radius also represents the radius for which $\sim 95\%$ of the XMM-Newton sources in the SSC catalogue are associated with USNO A.2 sources (see Fig. 7.5 in the First XMM-Newton Serendipitous Source Catalogue: 1XMM, User Guide to the Catalogue).

Thirty-one X-ray sources have one or more optical counterparts brighter than $R \sim 24.0$ within the XMM-Newton error box, while for four objects there are no obvious counterparts down to the magnitude limits of the optical images (see Sect. 2.3). The probability threshold adopted in the X-ray detection algorithm corresponds to less than 1 spurious X-ray detection. We are then confident that also X-ray sources without optical counterparts are real X-ray sources and in the following we address to these objects as blank fields.

In Fig. 1 we report the displacements between the optical and X-ray positions as a function of the off-axis angle. As shown by the size of the symbols (increasing as the X-ray flux decreases), a better X-ray-optical matching is achieved for the X-ray brightest sources, generally characterized by the sharpest PSF. For these sources the displacements from the claimed optical counterparts are $< 2''$ even at large offaxis angles ($> 12'$). The average displacements (~ 2 arcsec) of the X-ray faintest sources are consistent with those expected at these flux levels (see above). We finally note that the residual

⁵ Deep Infrared Mosaicing Software, developed by P. Eisenhardt, M. Dickinson, A. Stanford and J. Ward, and available at <ftp://iraf.noao.edu/contrib/dimsumV2>

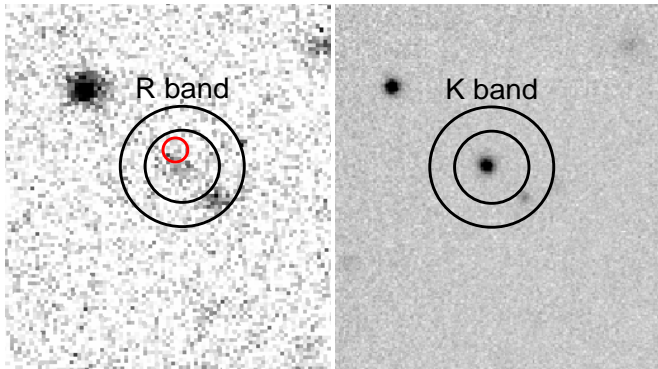


Fig. 2. (left panel) *R*-band image of source 127. The small 1'' circle represents the position of the source detected by *Chandra*; the 3'' and 5'' large circles are centered on the XMM-Newton position; (right panel) *K*-band image for source 127. See Sect. 5.1 for details.

astrometric differences between the X-ray and optical positions do not show any clear trend with the off-axis angle between 4 and 11 arcmin, where the bulk of the sources are detected.

For each of the 29 XMM-Newton sources covered by radio observations we also searched for radio sources within the X-ray error box (5'' radius). We found 5 X-ray/radio associations, while for the remaining 24 X-ray sources we report the 3σ upper limit (see Table 1).

3.1. Confusion problems

The additional *Chandra* data of the PKS 0312-77 field allowed us to quantitatively investigate confusion problems of X-ray sources, i.e. when the measured X-ray emission is indeed originated from two or more X-ray sources at a distance comparable to the XMM-Newton PSF. This could in principle be the case for four out of 31 sources, for which two candidate optical counterparts fall within the XMM-Newton error circle (sources 20, 22, 127, and 18). Only in one case (source 18, also known as P3 [F00]) two objects are clearly resolved by *Chandra* within the XMM-Newton detection (see Fig. 1 in Comastri et al. 2002a); the X-ray flux of the faintest source is only about 10% of the claimed counterpart, suggesting that most of the XMM-Newton flux belongs to P3. The subarcsec positional accuracy of *Chandra* allows to unambiguously identify the correct optical counterparts of the remaining three sources and to exclude that two individual X-ray sources contribute to the measured XMM-Newton flux (see Fig. 2 for an example).

The multiwavelength coverage of our survey turned out to be extremely useful to investigate confusion problems also for the sources for which *Chandra* data are not available. The closest optical counterpart of source 35 ($R = 22$), at a distance of $\sim 4''$ from the X-ray centroid, has been identified with a Broad Line AGN at $z = 1.272$; given the AGN surface density at these faint optical magnitudes ($\sim 100 \text{ deg}^{-2}$ at $R = 22$, assuming a $B-R$ color of 0.6; Koo & Kron 1988), the corresponding probability that the source lies entirely by chance in the XMM-Newton error box is 6.0×10^{-4} . However, a relatively bright ($S_{5 \text{ GHz}} \sim 0.4 \text{ mJy}$) radio source, associated with an optically

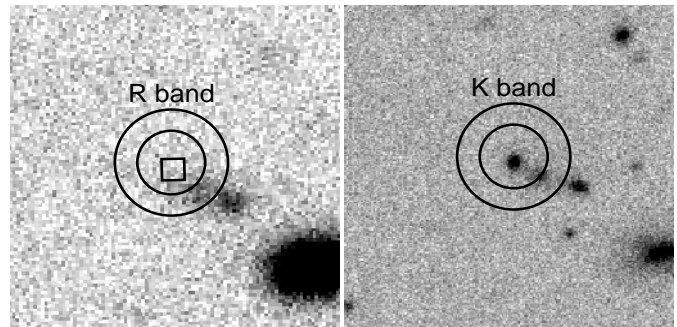


Fig. 3. (left panel) *R*-band image of source 35. The small 1.5'' width box represents the radio detection position, the 3'' and 5'' large circles are centered on the XMM-Newton position; (right panel) *K*-band image for source 35. See Sect. 3.1 for details.

blank field ($R > 24.6$, see Fig. 3) is almost coincident with the X-ray centroid. A bright ($K = 18.5$) source clearly emerges in the infrared band at the position of the radio source; the $R-K$ color > 5.1 places this source among the Extremely Red Object (ERO; $R - K > 5.0$) population. Given the EROs surface density at $K < 18.5$ ($\sim 800 \text{ deg}^{-2}$, Daddi et al. 2000) and the fraction of radio-emitters EROs at this level ($< 10\%$, see, e.g., Smail et al. 2002; Roche et al. 2003) the corresponding probability that a radio emitting ERO lies entirely by chance in the XMM-Newton error box is $< 5.0 \times 10^{-4}$. It is then likely that both the Broad Line AGN and the ERO contribute to the measured X-ray emission, although on the basis of the chance coincidence argument we are not able to definitely disentangle the contribution of each source; therefore, we have associated half of the X-ray flux to the Broad Line AGN and half to the ERO. We also note that the above described uncertainty in the source classification cannot be solved making use of the X-ray to optical flux ratio. Indeed even changing the X-ray flux by a factor two the rest-frame f_X/f_{opt} would be consistent with the typical values observed for broad line AGN and EROs respectively (in the latter hypothesis the redshift has been estimated from the $K-z$ relation of radiogalaxies).

3.2. Sources at distance $> 3''$

Twenty-five out of 31 sources in the present sample show optical counterparts within a 3'' radius from the XMM-Newton centroid. The probability P of chance coincidence is in all cases, but one (see Table 1), lower than 0.01 ($P = 1 - e^{-\pi r^2 n(m)}$, where $n(m)$ is derived from the number magnitude relation of field galaxies reported by Pozzetti & Madau 2000), strongly supporting the reliability of our identifications. The *Chandra* and radio detections turned out to be extremely useful to identify five out of the six remaining sources for which the closest optical counterpart lies between 3 and 5 arcsec from the XMM-Newton centroid (Fig. 4):

- the optical counterpart of source 29 ($r \approx 3''$) is a galaxy very close to a bright F/G star; it lies at $\sim 1.5''$ from a *Chandra* source and it is most likely the correct identification.

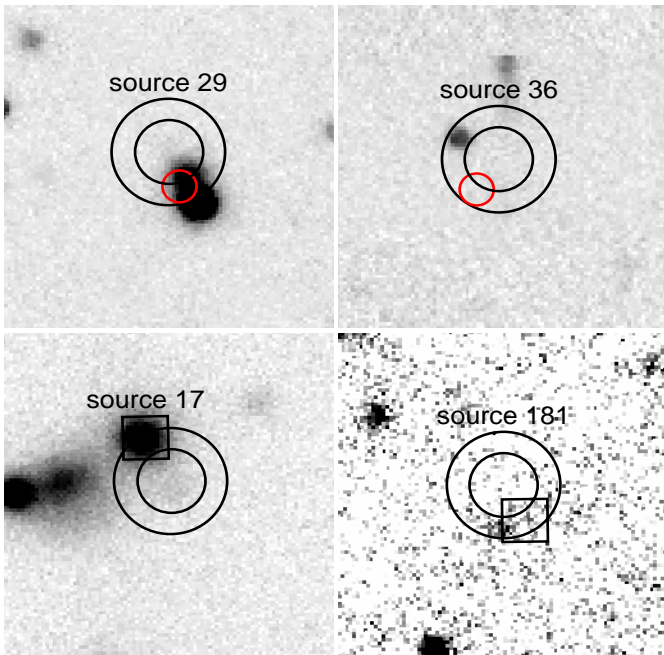


Fig. 4. EFOC2 R-band images of 4 sources at a distance $> 3''$ from the XMM-Newton centroid. The $3''$ and $5''$ large circles are centered on the XMM-Newton position. (*top panels*) sources 29 and 36: the small circles refer to the Chandra centroid and indicate a radius of $1.5''$; (*bottom panels*) source 17 and 181: the squares refer to the radio centroids ($4''$ width). See Sect. 3.2 for details.

- a Chandra source within the XMM-Newton error box of source 36 lies at $\sim 4.8''$ from the possible optical counterpart which therefore cannot be the correct identification (see Fig. 4). In the following we refer to this source as an optically blank field.
- the radio detection of the optical counterpart of source 17 ($r = 4.5''$) strongly suggests that the identification is secure;
- a faint radio source, detected at the 3.5σ level at $\sim 3''$ from the nearest optical counterpart of source 181 is likely to be the correct identification given the uncertainty on the radio position ($2\text{--}3''$)
- source 35 has been already discussed in the previous subsection.

The remaining object (source 66) is associated with a faint optical counterpart ($R = 23.1$), classified as a Broad Line AGN, at a distance of $3.7''$. Given the AGN surface density at these faint magnitudes ($\sim 300 \text{ deg}^{-2}$, Mignoli et al. 2002) the probability of chance coincidence is 1.8×10^{-3} ; we are therefore confident that the identification is correct.

Summarizing, we have securely identified 29 X-ray sources with a unique optical counterpart; in one case (source 35, see Sect. 3.1) we cannot provide a unique identification. Five X-ray sources turned out to be optically blank fields at the limit of our images.

The relative shifts between X-ray and optical centroids are plotted in Fig. 5 (*left panel*) and also reported in Table 1.

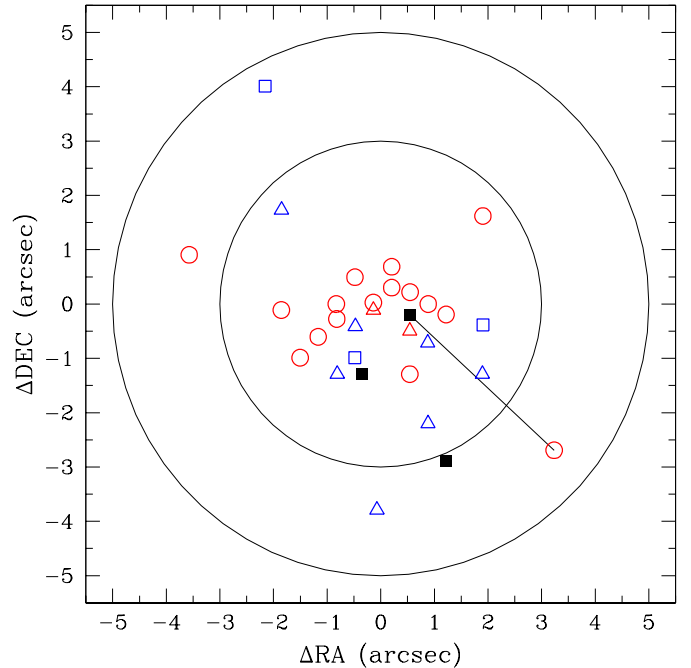


Fig. 5. Displacement between optical and X-ray positions of the proposed optical counterparts of the X-ray sources in the PKS 0312-77 field, after the astrometric calibration. Symbols are as follows: open circles are Broad Line AGNs, open triangles are Narrow Emission-line objects (Narrow Line AGNs and ELGs), empty squares are galaxies, and filled squares are spectroscopically unidentified sources. The solid line connects the two possible counterparts of source 35 (see Sect. 3.1). The circles refer to the XMM-Newton error circles of $3''$ and $5''$, respectively.

3.3. Spectroscopic breakdown

We have obtained good quality optical spectra for 28 out of 30 objects with $R < 24$. The optical counterparts have been classified into three broad categories:

- **Broad Line AGN (BL AGN):** sixteen objects having broad emission lines ($FWHM \gtrsim 2000 \text{ km s}^{-1}$).
- **Narrow Emission Line Galaxies (NELGs):** nine objects including both narrow-line Type 2 AGN with $FWHM \lesssim 2000 \text{ km s}^{-1}$ or high-ionization state emission lines, and extragalactic sources without obvious AGN features in their optical spectra but with the presence of at least one, strong emission feature (Emission Line Galaxies, ELGs).
- **Normal galaxies** three objects showing a red continuum and an absorption line optical spectrum, typical of an early-type elliptical galaxy.

4. Radio properties

We have found five X-ray/radio associations out of 29 sources with radio coverage. The 5 GHz flux versus the R band magnitude is reported in Fig. 6. The dot-dashed line shows the value of $\alpha_{\text{ro}} = 0.35$, often used to separate Radio Loud (RL) and Radio Quiet (RQ) objects (see Ciliegi et al. 2003 for details). Three out of the 5 X-ray/radio associations were clearly detected at fluxes higher than 1 mJy. It is interesting to note that

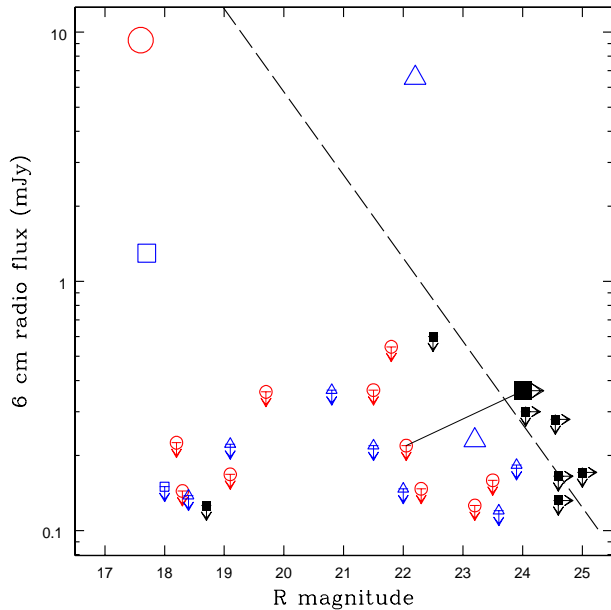


Fig. 6. The 5 GHz flux vs. R -band magnitude for the 29 sources with radio coverage. The dashed line represents the locus of $\alpha_{\text{to}} = 0.35$ (see text for details). Symbols are as in Fig. 5. The solid line connects the two possible counterparts of source 35 (see Sect. 3.1). Enlarged symbols represent radio detections.

these radio-bright sources show heterogeneous optical properties. Only one object (source 16), spectroscopically identified with an ELG at $z = 0.84$, is classified as RL according to its α_{to} . The high-level of radio emission and its hard X-ray color (see Sect. 5.2) allow us to classify it as a Narrow Line Radio Galaxy, the only flavor of obscured Type 2 AGN which has been extensively studied at all redshifts and over a wide range of luminosities (e.g. McCarthy 1993). The brightest radio source ($S_{5 \text{ GHz}} = 9.3 \text{ mJy}$) is source 2, spectroscopically identified with a BL AGN (see also F00). Even if this object would not be classified as a RL source on the basis of the observed α_{to} , the 5 GHz luminosity of $\sim 10^{26} \text{ Watt Hz}^{-1}$ is typical of RL quasars ($> 10^{24} \text{ Watt Hz}^{-1}$). Finally, a detailed discussion on the nature of the third bright object, an absorption line galaxy (source 17), is postponed to Sect. 5.3.

At fluxes below 1 mJy, we have detected radio emission in two sources (source 35 and source 181).

As discussed in Sect. 3.1, a radio source is almost coincident with the XMM-Newton centroid of source # 35. On the basis of its α_{to} value, this object would be classified as a RL object. If the K - z relation (Jarvis et al. 2001) of powerful radio galaxy holds also at the mJy flux level, its bright K -band emission ($K \sim 18.5$, see Fig. 3) suggests that this object could be a high-redshift ($z = 1.5$ – 2) galaxy.

Finally, source 181 is classified as an ELG on the basis of the optical spectrum.

Given the small area sampled and taking into account the radio coverage, the present X-ray sample is not suitable for a reliable estimate of the RL fraction among X-ray selected samples and a detailed analysis based on a larger statistic is deferred to a forthcoming paper (Ciliegi et al., in preparation).

5. Discussion

5.1. Broad-line objects

The 16 objects with broad optical emission lines have an average X-ray-to-optical flux ratio $\langle \lg(F_{\text{X}}/F_{\text{R}}) \rangle = 0.32$ with a dispersion of 0.48 (see Fig. 7, left panel) which is typical of soft X-ray selected Type 1 AGN (Lehmann et al. 2001).

Given the high spectroscopic completeness of the present sample, it is possible to place some constraints on the intrinsic column density (N_{H}) directly from the HR vs. z diagram (Fig. 7, right panel). While a population of BL AGNs with an unobscured X-ray spectrum is present at all redshifts and spans a wide range in luminosities, several examples of X-ray obscured, BL AGNs seem to be present at high redshifts and X-ray luminosities. Taking the absorption column density obtained from the HR analysis at the face value, six out of the 13 BL AGNs with $L_{\text{X}} > 10^{44} \text{ erg s}^{-1}$ (Fig. 8) would have $N_{\text{H}} > 10^{22} \text{ cm}^{-2}$, and two even larger than 10^{23} cm^{-2} (Fig. 7, right panel).

Since the HR technique provides only a rough estimate of the X-ray spectral properties, we have tried to constrain the intrinsic column density through proper spectral analysis. A detailed description of the X-ray spectral fitting results for all the 122 sources in the HELLAS2XMM sample is reported in Perola et al. (in preparation). Here we briefly discuss the results relevant for the purposes of this paper, and in particular the 6 BL AGN for which the HR analysis suggests the presence of significant X-ray absorption.

The source spectrum and associate background and response files for each of the 13 BL AGN (and for each XMM-Newton detector: *pn* and *MOS*) have been extracted from the original event files using the standard procedures with version 5.4 of the SAS. About half (six out of 13) of the sources are detected with a number of counts (< 150) which does not allow to adopt the standard χ^2 minimization technique. The use of the C-statistic, originally proposed by Cash (1979), is well suited to fit spectra with a few counts per bin in the limit of pure Poisson errors. In order to compare the results with those obtained with the HR technique (Fig. 7, left panel), the power-law slope has been fixed to $\Gamma = 1.8$. The only parameters free to vary are the source normalization and the rest-frame intrinsic column density. There is no indication of intrinsic absorption for all of the seven sources which were considered as unobscured on the basis of their HR. The same conclusion has been reached for two out of the six BL AGN classified as X-ray obscured from their HR (source #35 and #21), though the absorption inferred from the HR is consistent with the upper limit obtained from the spectral analysis. For three of them (#127, #22 and #66), the best-fit rest-frame N_{H} values are 17, 4.8, $4.7 \times 10^{22} \text{ cm}^{-2}$, respectively, and larger than $\sim 10^{22} \text{ cm}^{-2}$ at 90% confidence level for all the sources. These values are fully consistent with those obtained from the HR and provide further evidence toward the presence of substantial absorption in these objects.

The brightest X-ray obscured ($N_{\text{H}} \sim 10^{22} \text{ cm}^{-2}$ from the HR) BL AGN (source # 7) has been detected with enough counts to constrain both the power-law slope and the

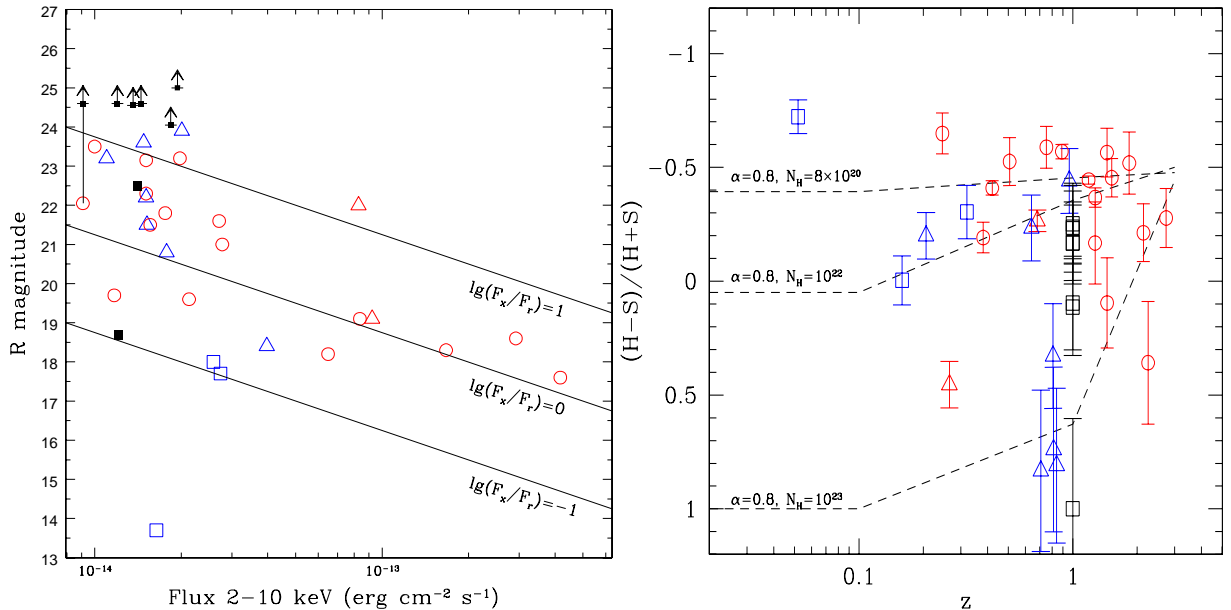


Fig. 7. (*Left panel*) R -band magnitude vs. 2–10 keV X-ray flux; the lines indicate the loci of constant X-ray-to-optical flux ratio (see Hornschemeier et al. 2000 for its definition). Symbols as in Fig. 5. The solid line connects the two possible counterparts of source 35 (see Sect. 3.1); (*Right panel*) Hardness ratio as a function of redshift. Unidentified sources have been plotted at $z = 1$. For source 35, only the BL AGN counterpart has been plotted.

absorption column density. The best-fit parameters are fully consistent with the values published by Piconcelli et al. (2002). The power law slope is rather flat ($\Gamma \simeq 1.4$) and the 90% upper limit on the intrinsic absorption is about $3.5 \times 10^{21} \text{ cm}^{-2}$. If the power-law slope is fixed at $\Gamma = 1.8$, the quality of the fit is slightly worse ($\Delta\chi^2 = 3.1$ for 1 d.o.f.) with a best-fit $N_{\text{H}} = 3 \pm 2 \times 10^{21} \text{ cm}^{-2}$.

In order to assess the robustness of our procedure we have performed some tests. First of all, we have changed the size of the local background regions to search for possible background fluctuations. Then we fit simultaneously the source plus background and background datasets linking together the model parameters for the background spectrum. Finally, for the “brightest” sources (>150 net counts) we have employed the standard χ^2 fitting procedure. In all the cases, the best fit parameters agree each other within the statistical errors.

It is concluded that the absorption column densities inferred from the observed HR are slightly overestimated. Nevertheless, there are evidences of substantial intrinsic obscuration in three high-redshift sources spectroscopically classified as broad line AGN. The presence of broad optical emission lines and absorbed X-ray spectra can be explained either by a dust-to-gas ratio significantly different from the Galactic one (Maiolino et al. 2001) or by geometrical effects such as a patchy X-ray absorbing medium on the same scale of the broad line region.

The red optical-UV continua of some of the BL AGN in our sample suggest a dominant contribution of the host galaxy starlight or an intrinsically absorbed continuum. In this respect, the optical near-infrared properties of two objects in our sample are particularly interesting.

In source 7 ($z = 0.381$), the presence of a broad $H\alpha$ line and the relatively high X-ray luminosity ($\sim 2 \times 10^{44} \text{ erg s}^{-1}$), coupled with a red optical continuum dominated by the host

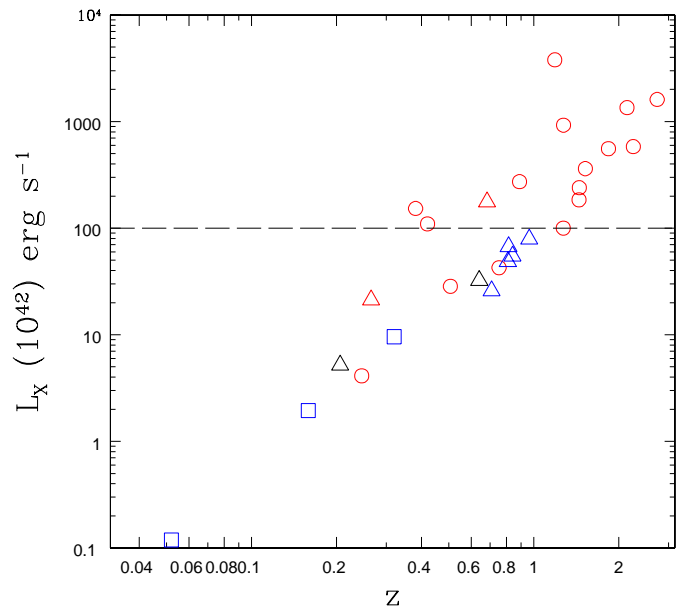


Fig. 8. The luminosity-redshift plane for all the identified sources in the PKS 0312–77 field. Symbols are as in Fig. 5. X-ray luminosities are corrected for absorption. High(Low)-luminosity objects lie above(below) the dashed line at $L_x = 10^{44} \text{ erg s}^{-1}$.

galaxy starlight (as the presence of Ca H and K plus other absorption lines clearly indicate, Fig. 9, *upper panel*), suggest to classify this object as a *red quasar*. Other examples of low-redshift red quasars have been discovered both in X-ray (Kim & Elvis 1999; Vignali et al. 2000) and near-infrared surveys (Wilkes et al. 2002). It is puzzling that, although moderate X-ray absorption ($N_{\text{H}} \simeq 10^{21-22} \text{ cm}^{-2}$) is often detected among red quasars, there is only marginal evidence of obscuration in

Table 1. Multiwavelength properties of the X–ray sources detected in the XMM–*Newton* observations.

ID	XMM position		$\Delta_{\text{XMM-opt}}$ [$''$]	$\Delta_{\text{Chandra-opt}}$ [$''$]	P	$S_{5\text{ GHz}}$ [mJy]	R	F_{2-10} [10^{-14} cgs]	HR	z	Class
	RA	Dec									
12	03 15 29.36	-76 53 41.61	2.50	... ^a	<0.01	...	21.0	2.78 ± 0.74	-0.52 ± 0.10	0.507	AGN 1
20	03 14 16.76	-76 55 59.51	2.37	1.42	<0.01	<0.219	21.5	1.52 ± 0.47	-0.44 ± 0.14	0.964	ELG
10	03 14 16.36	-76 45 36.51	0.69	2.60 ^b	<0.01	...	19.6	2.13 ± 0.61	-0.65 ± 0.09	0.247	AGN 1
22	03 13 48.96	-76 45 59.41	1.31	0.31	<0.01	...	21.6	2.71 ± 0.58	-0.21 ± 0.13	2.140	AGN 1
36	03 13 43.55	-76 54 26.26	3.47	4.77	0.013	<0.165	>24.6	1.45 ± 0.47	-0.23 ± 0.19
13	03 13 34.26	-76 48 29.71	0.86	0.66	<0.01	<0.360	19.7	1.17 ± 0.38	-0.56 ± 0.11	1.446	AGN 1
3	03 13 14.66	-76 55 55.81	1.23	1.04	<0.01	<0.150	18.3	16.72 ± 1.03	-0.41 ± 0.03	0.420	AGN 1 [†]
5	03 13 11.96	-76 54 29.71	1.40	0.64	<0.01	<0.168	19.1	8.37 ± 0.68	-0.37 ± 0.04	1.274	AGN 1 [†]
127	03 12 57.96	-76 51 20.31	0.36	0.55	<0.01	<0.159	23.5	1.00 ± 0.29	0.36 ± 0.27	2.251	AGN 1
65	03 12 52.16	-77 00 59.51	... [*]	... [*]	...	<0.300	>24.0	1.84 ± 0.51	0.11 ± 0.21
6	03 12 53.96	-76 54 14.51	0.73	0.70	<0.01	<0.150	22.0	8.28 ± 0.66	-0.26 ± 0.05	0.683	AGN 2 [†]
18	03 12 39.26	-76 51 32.61	1.94	1.29	<0.01	<0.150	18.0	2.59 ± 0.39	0.00 ± 0.11	0.159	GAL [†]
8	03 12 31.16	-76 43 24.01	1.10	0.62	<0.01	...	13.7 ^e	1.64 ± 0.52	-0.72 ± 0.07	0.0517	GAL/ group?
			2.90	1.49						0.0537	
			2.16	2.15						0.0517	
4	03 12 09.16	-76 52 13.01	0.14	0.60	<0.01	<0.225	18.2	6.49 ± 0.56	-0.57 ± 0.03	0.890	AGN 1 [†]
16	03 12 00.36	-77 00 25.61	0.63	1.33	<0.01	6.545 ± 0.500	22.2	1.51 ± 0.46	0.81 ± 0.34	0.841	ELG
89	03 11 44.96	-76 56 45.01	2.29	1.13	0.054	<0.150	23.6	1.48 ± 0.37	0.33 ± 0.23	0.809	ELG
181	03 11 35.96	-76 55 55.81	3.79	... ^c	0.104	0.230 ± 0.050	23.2	1.10 ± 0.32	0.83 ± 0.35	0.709	ELG
35	03 11 31.76	-77 00 36.31	4.21	... ^a	0.048	<0.360	22.0	1.83 ± 0.53	-0.17 ± 0.18	1.272	AGN 1
			0.60 ^b	... ^a	...	0.364 ± 0.073	>24.6		
66	03 11 28.16	-76 45 16.31	3.68	... ^d	0.09	...	23.1	1.51 ± 0.46	0.09 ± 0.20	1.449	AGN 1
17	03 11 24.76	-77 01 39.01	4.55	... ^a	<0.01	1.298 ± 0.088	17.7	2.74 ± 0.60	-0.30 ± 0.13	0.320	BL Lac
31	03 11 13.86	-76 53 59.11	... [*]	... [*]	...	<0.150	>24.6	1.20 ± 0.33	-0.17 ± 0.16
29	03 11 13.36	-76 54 31.11	3.13	1.57	<0.01	<0.150	18.7	1.21 ± 0.33	-0.24 ± 0.16
11	03 11 12.76	-76 47 01.91	1.86	1.50	<0.01	<0.366	21.5	1.56 ± 0.49	-0.59 ± 0.09	0.753	AGN 1
9	03 11 05.56	-76 51 58.01	0.89	0.13	<0.01	<0.150	23.2	1.98 ± 0.38	-0.45 ± 0.08	1.522	AGN 1
7	03 10 49.96	-76 39 04.01	0.83	... ^a	<0.01	...	18.6	29.2 ± 3.10	-0.19 ± 0.07	0.381	AGN 1
21	03 10 49.76	-76 53 16.71	0.72	0.24	<0.01	<0.150	22.3	1.51 ± 0.36	-0.28 ± 0.13	2.736	AGN 1
28	03 10 37.36	-76 47 12.71	2.53	1.09	<0.01	<0.366	20.8	1.78 ± 0.46	-0.23 ± 0.14	0.641	ELG
45	03 10 18.96	-76 59 57.91	... [*]	... ^a	...	<0.171	> 25.0	1.94 ± 0.57	0.09 ± 0.20
2	03 10 15.76	-76 51 33.21	0.59	0.64	<0.01	9.284 ± 0.073	17.6	41.6 ± 1.60	-0.44 ± 0.02	1.187	AGN 1 [†]
124	03 10 01.60	-76 51 06.71	1.33	1.88	<0.01	<0.300	22.5	1.41 ± 0.45	-0.25 ± 0.18
501	03 09 52.16	-76 49 27.41	... [*]	... ^a	...	<0.279	>24.5	1.36 ± 0.45	1 ± 0.40 ^f
14	03 09 51.16	-76 58 24.71	1.52	... ^a	<0.01	<0.150	18.4	3.97 ± 0.70	-0.20 ± 0.10	0.206	Starburst
24	03 09 31.66	-76 48 45.01	1.80	... ^a	<0.01	<0.546	21.8	1.76 ± 0.54	-0.52 ± 0.13	1.838	AGN 1
116	03 09 18.46	-76 57 59.31	1.13	... ^a	0.017	<0.183	23.9	2.01 ± 0.67	0.74 ± 0.36	0.814 ^g	ELG
34	03 09 12.06	-76 58 25.91	0.17	... ^a	<0.01	<0.222	19.1	9.24 ± 1.13	0.45 ± 0.10	0.265	AGN 2

* Blank field; ^a out of *Chandra* ACIS-I field; ^b at the edge of ACIS field; ^c CCD gap; ^d not detected; ^e: the R -band magnitude refer to the three nuclei altogether (see §5.3); ^f: we note that a $R = 20.1$ counterpart lies at $5.9''$ from the XMM centroid; ^g redshift based on a single faint line; [†]: sources reported in Fiore et al. (2000).

However, a more complicate scenario for the two sources in our sample is suggested on the basis of multiwavelength data.

A detailed study of source 18, which can be considered the prototype of this class of objects, has been already reported in Comastri et al. (2002a): the low level of radio emission and the broad-band spectral energy distribution favour the presence of an heavily obscured, possibly Compton-thick ($N_{\text{H}} > 1.5 \times 10^{24} \text{ cm}^{-2}$) Seyfert-like nucleus.

Alternatively, XBONGs could be the host galaxies of BL Lac objects; if this were the case, deep radio observations would be the most useful tool to test this possibility. The relatively strong radio emission of source 17 ($S_{5\text{ GHz}} \sim 1.3 \text{ mJy}$) and the relatively unobscured X–ray spectrum ($N_{\text{H}} \sim 10^{21} \text{ cm}^{-2}$) favours the BL Lac hypothesis. Furthermore, for source 17, the 5 GHz luminosity ($\sim 3 \times 10^{40} \text{ erg s}^{-1}$), which is considered a good indicator of the overall spectral energy

distribution (see Fig. 7a in Fossati et al. 1998), suggests that this object could be a rather extreme example of a high-energy peaked BL Lac (HBL; Ghisellini et al. 1998; Costamante et al. 2001). This also explains the dominance of the stellar continuum over the BL Lac non-thermal emission in the optical band. For comparison, a few examples of radio bright XBONGs have been recently reported by Gunn et al. (2003) in the 13hr XMM-Newton field.

The third object (source 8) is the softest source in the sample ($HR = -0.72$) and is also characterized by the lowest X-ray-to-optical flux ratio ($\langle \lg(F_x/F_R) \rangle \sim -2.5$). Deep R -band image revealed a complex morphology: the peak of the X-ray emission is almost coincident with the brightest nucleus of an interacting system at $z \sim 0.05$ containing at least three nuclei in a common envelope. The total R -band magnitude of the system is $R = 13.7$. The optical spectra of the three nuclei are very similar, showing an absorption-line spectrum typical of early-type galaxies, without any emission line except for a weak $H\alpha$ in the faintest one. Both the optical and X-ray data favour thermal emission from a small group of galaxies. The quality of the present XMM-Newton observation, however, does not allow to distinguish between point-like and extended X-ray emission. Unfortunately, the source lies at the edge of the ACIS-I field in the *Chandra* observation, leaving this issue unsettled. Alternatively, if the X-ray emission were associated with a single nucleus, this object would be more similar to the previously discussed XBONGs.

5.4. Unification schemes, absorbed X-ray sources, and the XRB

Recent multiwavelength programs of follow-up observations of hard X-ray selected sources have already revealed a complex nature for the hard X-ray source population (Barger et al. 2002, Giacconi et al. 2002; Willott et al. 2003). They have also suggested the necessity for substantial revision of the AGN unification models, which in their simplest version (e.g., Antonucci 1993), predict a one-to-one relation between optical type 1 and X-ray unobscured sources, and between optical type 2 and X-ray obscured sources. Despite the relatively low number of objects and the small area covered, the high spectroscopic completeness ($\sim 80\%$) and the multiwavelength coverage of the PKS 0312-77 field allow to further investigate this issue. As far as Seyfert luminosities ($L_x \lesssim 10^{44}$ erg s $^{-1}$) are concerned, our findings are in agreement with the prediction of current unification models: the narrow-line AGNs are typically X-ray obscured, while the BL AGNs are not.

There seem to be, however, some hints for a departure from this simple scheme when quasar luminosities are considered; for example, the inferred column densities of three type 1 QSOs are significantly higher than those estimated from the optical reddening indicators assuming a Galactic extinction curve (see Sect. 5.1).

Other examples of X-ray absorbed, BL AGNs (both Seyfert and QSOs) have been discovered at relatively low redshifts among AGN selected from near-infrared surveys (2MASS AGN survey, Wilkes et al. 2002) and at brighter X-ray fluxes

in the ASCA and *BeppoSAX* surveys (Akiyama et al. 2000; Fiore et al. 2001a,b; Comastri et al. 2001). Although it seems premature to claim that a population of X-ray obscured type 1 AGN has been discovered, it is interesting to note that, if a sizeable number of these objects will be found by more sensitive X-ray observations, they could have the same role in contributing to the XRB of the so far elusive class of QSO2, for which only a handful of objects are reported in literature (e.g., Stern et al. 2002; Norman et al. 2002; Mainieri et al. 2002). For the five objects undetected in the optical images, no reliable spectroscopic identification is possible even with 8 m class telescopes. These objects are characterized by an X-ray-to-optical (hereinafter X/O) flux ratio > 10 , e.g. more than one order of magnitude larger than the value expected for optically selected AGNs (Lehmann et al. 2001). Sources with such a high X/O ratio represent $\sim 25\%$ of the present sample (9 objects, see Fig. 7) and their fraction seems to be constant at lower fluxes in deep *Chandra* and XMM-Newton observations (see Fiore et al. 2003 for a detailed discussion). A large fraction of high X/O ratio sources is characterized by intrinsic column densities in excess of 10^{22} cm $^{-2}$. This is an indication that the majority of the high X/O are powered by an X-ray obscured AGN. As shown in Fiore et al 2003 (see their Sect. 5 for details), it has been proposed that a large fraction of these sources would lie in the redshift range $z = 0.5 \div 2$. If this were the case, at the fluxes of the present survey, high X/O sources would have an X-ray luminosity larger than 10^{44} erg s $^{-1}$ and would contribute to increase the fraction of high-luminosity, highly obscured sources closer to that predicted by XRB models.

Moreover, preliminary results on VLT/ISAAC K -band imaging of high X/O sources revealed that almost all of the optically blank fields are associated with Extremely Red Objects (Mignoli et al. 2003), further supporting the high-redshift nature for these objects. Deep K -band spectroscopy would definitively test this hypothesis.

6. Summary

The most important results obtained from the extensive multiwavelength coverage of the HELLAS2XMM field surrounding the radio-loud quasar PKS 0312-77 can be summarized as follows:

- We have detected 35 serendipitous hard X-ray sources in a 30 ks XMM-Newton observation in the field of the radio loud-quasar PKS 0312-77. The X-ray sources span the flux range between $1 \div 40 \times 10^{-14}$ erg cm $^{-2}$ s $^{-1}$.
- Thanks to the extremely good positional accuracy of *Chandra*, complemented by medium-deep radio and K -band observations, we have unambiguously identified the optical counterparts of $\sim 85\%$ of the hard X-ray selected sources. Taking into account the *Chandra* coverage of the XMM-Newton field, coupled with radio and infrared data we have revealed confusion problems in 2 out of 35 sources ($\sim 6\%$) at an X-ray flux level of about 10^{-14} erg cm $^{-2}$ s $^{-1}$.
- At the relatively bright 2-10 keV fluxes sampled by our survey, the identified objects are characterized by a wide spread in their optical properties (both in the continuum

shape and emission lines). The overall picture emerging from our study suggests that the optical appearance of hard X-ray selected AGN is different from what expected on the basis of the unified schemes, implying that classification schemes may not apply beyond the waveband in which they were made.

- Optical spectra of X-ray absorbed sources have revealed a few examples of high-redshift, high-luminosity objects optically classified as BL AGNs.
- The multiwavelength coverage of the three “normal”, X-ray bright galaxies made possible to further investigate the nature of this class of objects. Thanks to deep radio data, it was possible to tentatively identify a (H)BL Lac as the nuclear source of one object (source 17); the multiwavelength properties of source P3 have been already extensively discussed (Comastri et al. 2002a) and favour a Compton-thick scenario; the origin of the X-ray emission from the third object is probably related to thermal radiation from an interacting system.
- Finally, about 25% of the objects in the present sample have X-ray-to-optical flux ratio greater than 10. Our results support the hypothesis that high X/O sources are powered by obscured accretion at $z \sim 1$. Deep near-infrared spectroscopy could provide a powerful tool to test this scenario.

The overall picture of the nature of hard X-ray selected sources has already approached a fairly complicate description; it is clear that further and deeper observations over a broad range of frequencies would be helpful to better understand the content of hard X-ray sky.

Acknowledgements. We thank the entire *Chandra* team and in particular the CXC team for the support received in the data analysis. This paper used observations collected at the Australian Telescope Compact Array (ATCA), which is founded by the Commonwealth of Australia for operation as a National Facility by CSIRO. The authors acknowledge partial support by ASI I/R/113/01 and I/R/073/01 contracts. MB and AC thank G. Zamorani for useful comments and discussion. PS thanks the financial support from ASI I/R/037/01. CV also thanks the NASA LTSA grant NAG5-8107 for financial support. Last, but not least, comments by the referee greatly helped us to improve the presentation of the results.

Appendix A: Comparison with Lumb et al. (2001) and SSC sources

A list of serendipitous X-ray sources detected in the field of PKS 0312–77 was published by Lumb et al. (2001, hereinafter L01) and, more recently, by the SSC consortium. Here we try to investigate the differences in both the number of detected sources and their X-ray fluxes on the basis of the available information.

- L01: Using a sliding-cell detection algorithm (the XMM–SAS task EBOXDETECT) and a detection threshold of 5σ , 52 sources were detected in the soft (0.5–2 keV) band; for 47 of these sources the 2–10 keV flux was also reported.

- SSC: A total of 142 sources were detected in at least one of the five different energy bands (0.2–0.5; 0.5–2; 2–4.5; 4.5–7.5; 7.5–12 keV) and/or in one of the three EPIC cameras, with a maximum likelihood parameter (ML, from the task EBOXDETECT) larger than 8.

The comparison between our sample, L01 sample and SSC sample is not straightforward due to the different detection algorithms, thresholds, band selection and, partly, to the different versions of the analysis software adopted in the data reduction. We also note that the L01 results have been obtained on the basis of preliminary calibrated data.

There is a significant difference in the total number of X-ray detected sources. The origin of this discrepancy could be mainly ascribed to the hard X-ray selection of our sample. Twenty-seven of the 35 sources in our sample have been reported by L01; 32 of the 35 sources have also been detected by the SSC when the detection in the 2–4.5 keV band (the energy range closest to the 2–10 keV band where the signal-to-noise ratio is maximized) is considered. We note that all of the sources in common between L01 and our sample are also included in the SSC sample. The five sources which belong to our sample and the SSC catalogue only (#127, 65, 16, 89, and 45 in Table 1) are detected with $ML > 12$ in the SSC 2–4.5 keV band; therefore we consider these sources as highly reliable. The absence of these sources in L01 is likely due to their hard X-ray spectrum (all of them have $HR > 0$; see Table 1).

Three sources are reported in our catalogue (#181, 501, and 116) but not in the L01 and SSC ones; they are the hardest sources in our sample, and appear robust X-ray detections by visual inspection. The lack of these objects in the L01 and SSC sample is most likely due to the hard X-ray selection.

Four sources reported in L01 with fluxes brighter than our flux limit are not present in our sample, although they are included in the SSC catalogue. Their non-detections in the SSC 2–4.5 keV band and their soft X-ray colors (quoted in Table 1 of L01) justify their absence in our 2–10 keV sample.

We have also compared the flux measurements of individual objects detected above the limiting flux of our survey ($F_{2-10} \approx 10^{-14}$ erg cm⁻² s⁻¹) which are in common in the three samples reported above. Our investigation reveals that the L01 fluxes are typically lower than ours by ~25–30% at fluxes $\gtrsim 3 \times 10^{-14}$ erg cm⁻² s⁻¹ (see Fig. A.1, *left panel*). Since the fluxes in the two samples have been computed assuming the same spectral model ($\Gamma = 1.7$ and Galactic absorption), the differences are likely to be due to a different correction adopted for the encircled energy fraction. This is particularly pronounced for the bright sources detected at large off-axis angles (see, e.g., source #7). Two sources in the L01 sample deviate by more than one order of magnitude from our flux measurements (#34 and #66); we think that this is likely due to typos in Table 1 of L01.

Conversely, there is a good agreement between our fluxes and the SSC ones (see Fig. A.1, *right panel*) for the 32 common sources. This result gives further support to the reliability of our flux estimates. The SSC 2–10 keV fluxes have been computed using the summed count rates in the 2–4.5 and 4.5–7.5 keV

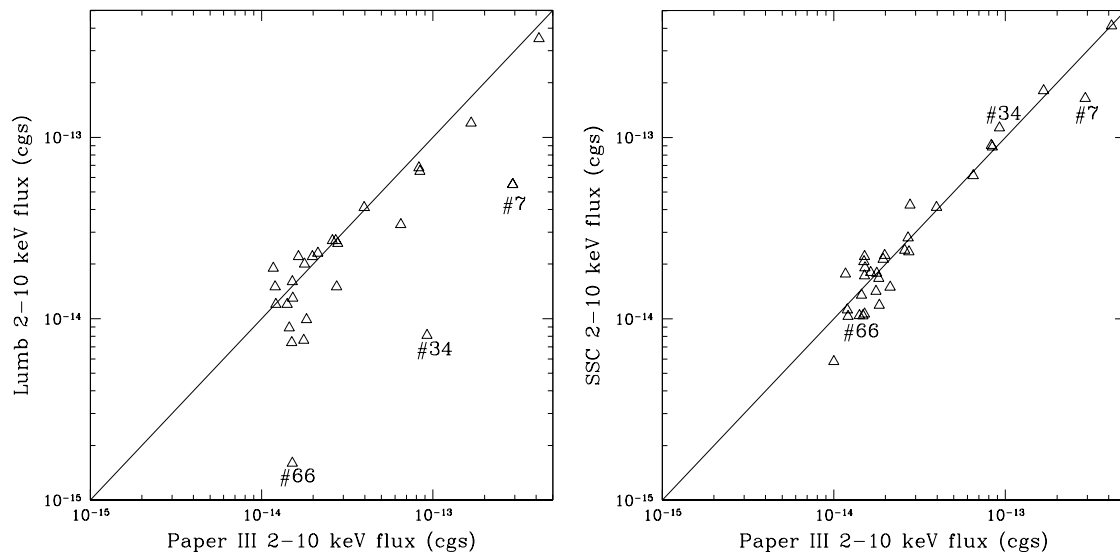


Fig. A.1. (*Left panel*) The comparison between the 2–10 keV fluxes of our sample and those estimated by L01 for the 27 common sources. The solid line represent the relation 1:1 between the two fluxes estimated. Three sources discussed in the Appendix are also shown in the plot. (*Right panel*) As the *left panel*, but for the 32 common sources in the SSC and our samples.

bands extrapolated to the 2–10 keV band assuming the same spectral model adopted in this paper.

References

- Akiyama, M., Ohta, K., Yamada, T., et al. 2000, *ApJ*, 532, 700
- Akiyama, M., Ueda, Y., & Ohta, K. 2002, in the AGN Surveys, Proc. of IAU Colloq. 184, ed R. F. Green, E. Ye. Khachikian, & D. B. Sanders, ASP, 284, 245
- Alexander, D. M., Brandt, W. N., Hornschemeier, A. E., et al. 2001, *AJ*, 122, 2156
- Alexander, D. M., Bauer, F. E., Brandt, W. N., et al. 2003, *AJ*, 126, 539
- Antonucci, R. R. J. 1993, *ARA&A*, 31, 473
- Baldi, A., Molendi, S., Comastri, A., et al. 2002, *ApJ*, 564, 190 (Paper I)
- Barcons, X., Carrera, F. J., Watson, M. G., et al. 2002, *A&A*, 382, 522
- Barger, A., Cowie, L., Mushotzky, R. F., & Richards, E. A. 2001, *AJ*, 121, 662
- Barger A., Cowie L., Brandt, W. N., et al. 2002, *AJ*, 124, 1839
- Bershady, M. A., Lowenthal, J. D., & Koo, D. C., 1998, *ApJ*, 505, 50
- Bertin, E., & Arnouts, S. 1996, *A&AS*, 117, 393
- Brotherton, M. S., Tran, H. D., Becker, R. H., et al. 2001, *ApJ*, 450, 559
- Brandt, W. N., Alexander, D. M., Hornschemeier, A. E., et al. 2001 *AJ*, 122, 2810
- Cagnoni, I., Della Ceca, R., & Maccacaro, T. 1998, *ApJ*, 493, 54
- Cash, W. 1979, *ApJ*, 228, 939
- Ciliegi, P., Vignali, C., Comastri, A., et al. 2003, *MNRAS*, 342, 575
- Comastri, A., Setti, G., Zamorani, G., & Hasinger, G. 1995, *A&A*, 296, 1
- Comastri, A. 2001, in X-ray Astronomy '99: Stellar Endpoints, AGNs and the Diffuse X-ray Background, ed. N.E. White, G. Malaguti, & G. G. C. Palumbo, AIP Conf. Proc., 599, p. 73
- Comastri, A., Mignoli, M., Ciliegi, P., et al. 2002a, *ApJ*, 571, 771 (Paper II)
- Comastri, A., Brusa, M., Ciliegi, P., et al. 2002b, in New Visions of the X-ray Universe in the XMM-Newton and Chandra Era, ESA SP-488, August 2002, ed. F. Jansen [astro-ph/0203114]
- Costamante, L., Ghisellini, G., Giommi, P., et al. 2001, *A&A*, 271, 512
- Daddi E., Cimatti, A., Pozzetti L., et al. 2000, *A&A*, 361, 535
- Dickey, J. M., & Lockman, F. J. 1990 *ARA&A*, 28, 215
- Fabbiano, G., Kim, D.W., & Trinchieri, G. 1992, *ApJS*, 80, 531
- Fiore, F., La Franca, F., Giommi, P., et al. 2000, *NewA*, 5, 143 (F00)
- Fiore, F., Antonelli, L. A., Ciliegi, P., et al. 2001, in X-ray Astronomy '99: Stellar Endpoints, AGNs and the Diffuse X-ray Background, ed. N. E. White, G. Malaguti, & G. G. C. Palumbo, AIP Conf. Proc., 599, 111
- Fiore, F., Giommi, P., Vignali, C. et al. 2001, *MNRAS*, 327, 771
- Fiore, F., Brusa, M., Cocchia, F. et al. 2003, *A&A*, 409, 79 (Paper IV), The First XMM-Newton Serendipitous Source Catalogue: 1XMM User Guide to the Catalogue, Release 1.2 15 April 2003, Associated with Catalogue version 1.0.1, Prepared by the XMM-Newton Survey Science Centre Consortium [<http://xmssc-www.star.le.ac.uk/>]
- Fossati, G., Maraschi, L., Celotti, A., Comastri, A., & Ghisellini, G. 1998, *MNRAS*, 299, 433
- Freeman, P. E., Kashyap, V., Rosner, R., & Lamb, D. 2002, *ApJS*, 138, 185
- Ghisellini, G., Celotti, A., Fossati, G., Maraschi, L., & Comastri, A. 1998, *MNRAS*, 301, 451
- Giacconi, R., Rosati, P., Tozzi, P., et al. 2001, *ApJ*, 551, 664
- Giacconi, R., Zirm, A., Wang, J., et al. 2002, *ApJS*, 139, 369
- Gilli, R., Salvati, M., & Hasinger, G. 2001, *A&A*, 366, 407
- Gunn, K. F., McHardy, I. M., Seymour, N., et al. 2003, *Astr. Nachr.*, 324, 105
- Hasinger, G., Altieri, B., Arnaud, M., et al. 2001, *A&A*, 365, L45
- Hornschemeier, A. E., Brandt, W. N., Garmire, G. P., et al. 2000, *ApJ*, 541, 49
- Jarvis, M. J., Rawlings, S., Eales, S., et al. 2001, *MNRAS*, 326, 1585
- Kim, D. W., & Elvis, M. 1999, *ApJ*, 516, 9
- Koo, D. C., & Kron R. G. 1988, *ApJ*, 325, 92
- Lehmann, I., Hasinger, G., Schmidt, M., et al. 2001, *A&A*, 371, 833
- Lumb, D. H., Guainazzi, M., & Gondoin, P. 2001, *A&A*, 376, 387 (L01)
- Madau, P., Ghisellini, G., & Fabian, A. C. 1994, *MNRAS*, 270, 17
- Mainieri, V., Bergeron, J., Hasinger, G., et al. 2002, *A&A*, 393, 425

- Maiolino, R., Marconi, A., Salvati, M., et al. 2001, *A&A*, 365, 28
- McCarthy, P. J. 1993, *ARA&A*, 31, 639
- Mignoli, M., Zamorani, G., & Marano, B. 2002, in *Lighthouses of the Universe, the most luminous celestial objects and their use for cosmology*, Proc. of the MPA/ESO/MPE/USM Joint Astronomy Conf., ed. M. Gilfanov, R. Sunyaev, & E. Churazov
- Mignoli, M., et al. 2003, in preparation (Paper V)
- Monet, D., Bird A., Canzian, B., et al. 1998, *The PMM USNO–A2.0 Catalog*, (Washington D.C: U.S. Naval Observatory)
- Moran, E. C., Filippenko, A. V., & Chornock R. 2002, *ApJ*, 579, L71
- Moorwood, A. F. M., Cuby, J.-G., Ballester, P., et al. 1999, *The Messenger*, 95, 1
- Mushotzky, R. F., Cowie, L. L., Barger, A. J., & Arnaud, K. A. 2000, *Nature*, 404, 459
- Norman, C., Hasinger, G., Giacconi, R., et al. 2002, *ApJ*, 571, 218
- Page, M. J., McHardy, I. M., Gunn, K. F., et al. 2003, *Astr. Nachr.*, 324, 101
- Patat, F. 1999, *Efosc2 Users' Manual*, LSO–MAN–ESO–36100–0004
- Piconcelli, E., Cappi, M., Bassani, L., et al. 2002, *A&A*, 394, 835
- Pozzetti, L. & Madau, P. 2000, in *The Extragalactic Infrared Background and its Cosmological Implications*, IAU Symp., 204, 71, ed. M. Harwit & M. G. Hauser, [astro-ph/0011359]
- Roche, N., Dunlop, J., & Almaini, O. 2003, *MNRAS*, submitted [astro-ph/0303206]
- Saracco, P., Giallongo, E., Cristiani, S., et al. 2001, *A&A*, 375, 1
- Setti, G., & Woltjer, L. 1989, *A&A*, 224, L21
- Severgnini, P., Caccianiga, A., Braitto, V., et al. 2003, *A&A*, 406, 483
- Smail, I., Owen, F. N., Morrison, G. E., et al. 2002, *ApJ*, 581, 844
- Stern, D., Moran, E. C., Coil, A. L., et al. 2002, *ApJ*, 568, 71
- Vignali, C., Mignoli, M., Comastri, A., Maiolino, R., & Fiore, F. 2000, *MNRAS*, 314, L11
- Ueda, Y., Takahashi, T., Ishisaki, Y., & Ohashi, T. 1999, *ApJ*, 524, L11
- Wilkes, B. J., Schmidt, G. D., Cutri, R. M., et al. 2002, *ApJ*, 564, L65
- Willott, C., Rawlings, S., Jarvis, M. J., & Blundell, K. M. 2003, *MNRAS*, 339, 397